

Positioning-Aided Channel Estimation for Multi-LEO Satellite Downlink Communications

Yuchen Zhang, Pinjun Zheng, Jie Ma, Henk Wymeersch, *Fellow, IEEE*, and Tareq Y. Al-Naffouri, *Fellow, IEEE*

Abstract—We investigate a multi-low Earth orbit (LEO) satellite system that simultaneously provides positioning and communication services to terrestrial user terminals. To address the challenges of channel estimation in LEO satellite systems, we propose a novel two-timescale positioning-aided channel estimation framework, exploiting the distinct variation rates of position-related parameters and channel gains inherent in LEO satellite channels. Using the misspecified Cramér-Rao bound (MCRB) theory, we systematically analyze positioning performance under practical imperfections, such as inter-satellite clock bias and carrier frequency offset. Furthermore, we theoretically demonstrate how position information derived from downlink positioning can enhance uplink channel estimation accuracy, even in the presence of positioning errors, through an MCRB-based analysis. To overcome the constraints of limited link budgets and communication rates associated with single-satellite-based communication, we develop a distributed beamforming strategy for downlink communication. This strategy allows LEO satellites to independently optimize their beamformers using local channel state information, eliminating the need for centralized processing while preserving the advantages of multi-satellite cooperative communication. Theoretical analyses and numerical results confirm the effectiveness of the proposed framework in achieving high-precision downlink positioning under practical imperfections, facilitating uplink channel estimation, and enabling efficient downlink communication.

Index Terms—LEO satellite positioning and communication, channel estimation, MCRB, distributed beamforming.

I. INTRODUCTION

The evolution of mobile communications has been driven by a remarkable vision: enabling seamless, high-speed information access from any point on Earth. While generational advances in cellular networks, from 1G to 5G and beyond, have largely achieved this goal in urban and suburban areas where infrastructure deployment is economically viable, significant challenges remain in rural and remote regions. In these underdeveloped areas, reliable communication and

internet access often remain either unavailable or prohibitively expensive, contributing to a growing digital divide [1]. The non-terrestrial networks (NTN)-based communications have emerged as a promising solution to bridge this gap, with airborne and spaceborne platforms such as high-altitude platform stations and satellites, serving as access points to enable truly global connectivity [2]. Among these candidates, low Earth orbit (LEO) satellites have attracted particular attention due to their distinct advantages over medium Earth orbit (MEO) and geostationary Earth orbit (GEO) satellites, including reduced path loss and propagation delay, greater constellation flexibility, and lower launch costs [3]–[5].

The advancement of LEO satellite-based global connectivity presents promising opportunities alongside significant challenges, particularly in channel estimation, a crucial aspect for meeting increasingly demanding high-speed communication requirements [6], [7]. While receivers can effectively mitigate channel aging by compensating for Doppler shift caused by rapid LEO satellite movement [3], [6], [8], the substantial propagation distance compared to terrestrial networks results in severe signal power attenuation. This attenuation particularly impacts pilot-based channel estimation methods, which struggle with low receive power, making effective channel state information (CSI) acquisition challenging, especially for power-constrained user terminals (UTs) such as mobile devices in the uplink. On the other hand, despite the reduced orbital altitude compared to MEO and GEO satellites, LEO communication links still span distances vastly exceeding typical terrestrial communication counterparts. This extended signal travel distance, combined with limited onboard power resources, significantly constrains the link budget of single-LEO satellite-based communication systems, creating a substantial barrier to achieving the ambitious throughput goals of wideband NTN communications [2], [7], [9].

Although satellite channels pose significant challenges for CSI acquisition, they exhibit distinct characteristics compared to terrestrial channels, particularly stronger line-of-sight (LOS) dominance and geometric properties [9]. These characteristics are inherently related to position information [5], suggesting that strategic utilization of UT position information could potentially address channel estimation challenges in LEO satellite communications, especially by enabling partial channel inference through the reconstruction of components such as steering vectors. However, this approach raises critical research questions, such as how to achieve accurate and efficient position acquisition within LEO satellite communication

This work is supported in part by the King Abdullah University of Science and Technology (KAUST) Office of Sponsored Research (OSR) under Award ORA-CRG2021-4695 and the European Commission through the Horizon Europe/JU SNS project Hexa-X-II under Grant Agreement no. 101095759.

Yuchen Zhang, Jie Ma, and Tareq Y. Al-Naffouri are with the Electrical and Computer Engineering Program, Computer, Electrical and Mathematical Sciences and Engineering (CEMSE), King Abdullah University of Science and Technology (KAUST), Thuwal 23955-6900, Kingdom of Saudi Arabia (e-mail: {yuchen.zhang; jie.ma; tareq.alnaffouri}@kaust.edu.sa).

Pinjun Zheng is with the School of Engineering, The University of British Columbia, Kelowna, BC V1V 1V7, Canada (e-mail: pinjun.zheng@ubc.ca). The majority of his contributions to this work were made during his Ph.D. studies at KAUST, Thuwal 23955-6900, Kingdom of Saudi Arabia.

Henk Wymeersch is with the Department of Electrical Engineering, Chalmers University of Technology, 41296 Gothenburg, Sweden (e-mail: henkw@chalmers.se).

networks and how to effectively leverage this position information to enhance LEO satellite channel estimation. On the other hand, to address the limited link budget of single-satellite systems, multi-satellite cooperative transmission has emerged as a promising solution [10]–[15]. However, achieving coherent transmission across satellites within non-orthogonal frequency or time resources presents significant challenges, such as phase synchronization among different satellites and the need for centralized processing based on global CSI [10]. These centralized operations introduce substantial processing overhead and latency, further complicating the practical implementation of cooperative transmission schemes.

The role of position information in terrestrial networks has been widely recognized for enhancing communication performance [16]–[20]. For instance, [16] introduces location awareness in 5G networks, demonstrating its potential for synchronizing coordinated communication schemes. Similarly, [17] showcases how position information facilitates beam alignment in millimeter-wave communication. These approaches typically rely on position information from either global navigation satellite system (GNSS) [16], [17] or radio sensing [18]–[20]. However, in LEO satellite scenarios, obtaining position information of terrestrial UTs through radar-like sensing at LEO satellites becomes impractical due to excessive round-trip signal attenuation. While GNSS appears to be a viable alternative, as demonstrated in [21], where UTs’ positions are obtained via GNSS and fed back to LEO satellites for downlink communication, the critical impact of positioning errors and the reliance on overidealistic synchronization assumptions remains under-explored and warrant further investigation in practical implementations.

Concurrent with advances in LEO satellite communication, there is growing interest in exploring LEO satellites as potential supplements or alternatives to GNSS [22], [23]. This interest arises from the inherent advantages of LEO satellites over GNSS, including stronger signal reception, extensive constellations, and broad frequency diversity, characteristics that have also partially driven the success of LEO satellite communications [23]–[25]. Recent research has begun to investigate the integration of LEO satellite communication and positioning functionalities. For instance, [26] proposes a massive multi-input-multi-output (MIMO) LEO satellite system that supports simultaneous communication and positioning in the downlink, designing hybrid beamforming to meet their distinct requirements. However, this work primarily focuses on the tradeoff between positioning and communication performance, overlooking their mutual benefits such as the potential of positioning in facilitating channel estimation, which is a critical challenge in LEO satellite systems. Moreover, it does not account for the inevitable clock bias and carrier frequency offset (CFO) among LEO satellites, factors that may significantly affect positioning performance.

Three key questions emerge under this context: 1) how can the positioning performance of LEO satellites be effectively characterized under practical imperfections such as clock bias

and CFO; 2) how can the position information of UTs obtained through LEO satellite positioning be leveraged to assist the challenging channel estimation task; and 3) how can the benefits of the improved link budget offered by multi-satellite cooperative communication be harnessed while avoiding the complexities of synchronization and centralized processing?

In this paper, we investigate a scenario where a cluster of LEO satellites, each equipped with a uniform planar array (UPA), simultaneously provides downlink positioning and communication services to multiple single-antenna terrestrial UTs. We aim to: 1) characterize the positioning performance under practical impairments such as clock bias/CFO incurred by imperfect time-/frequency-domain synchronization; 2) unveil how the UTs’ position information obtained by downlink positioning can be exploited to enhance uplink channel estimation; and 3) explore distributed beamforming relying solely on local CSI acquired at each satellite, enabling efficient downlink communication while avoiding the overhead and complexity typically associated with centralized operations. The main contributions of this paper are as follows.

- Building on the distinct variation rates of position-related parameters and random channel gains in LEO satellite channels, as detailed in Section II, we propose a two-timescale frame structure. Downlink positioning operates on the longer position-coherent timescale, while uplink channel estimation and downlink communication occur on the shorter channel gain-coherent timescale. Through this framework, each process is scheduled according to its variation rate, maximizing resource utilization while preserving the potential to leverage positioning for efficient channel estimation and communication.
- To characterize the LEO satellite-based positioning performance under imperfect inter-satellite clock bias and CFO, we employ misspecified Cramér-Rao bound (MCRB) theory rather than traditional Cramér-Rao bound (CRB) analysis. The MCRB framework is specifically designed to derive performance limits for estimation under model mismatch [27]. Through this theoretical approach, we rigorously analyze how imperfect inter-satellite clock bias and CFO affect time-of-arrival (TOA) and Doppler shift measurements, and systematically derive their impact on positioning accuracy.
- We demonstrate the advantage of leveraging the position information of UTs, obtained during the positioning stage, to enhance uplink channel estimation. Specifically, we account for the inevitable positioning errors, which introduce model mismatches in the positioning-aided channel estimation (PACE) process. By invoking the MCRB theory, we provide a theoretical characterization of the uplink channel estimation performance facilitated by the UTs’ position information.
- We propose a distributed beamforming strategy for downlink communication, where each UT is served by the LEO satellites with the cluster simultaneously. In this approach, each LEO satellite independently optimizes its

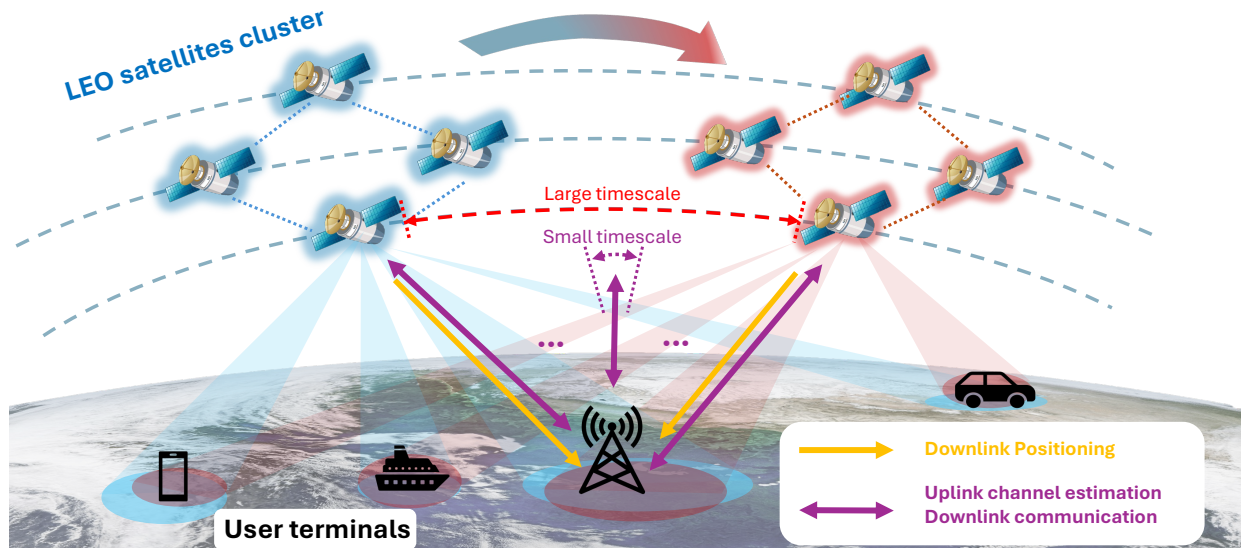


Fig. 1. A cluster of LEO satellites traverses orbit while simultaneously delivering positioning and communication services to UTs. Each UT is served by all LEO satellites within the cluster for both functionalities. Positioning operations in the downlink occur over a relatively large timescale, whereas uplink channel estimation and downlink communication are carried out on a smaller timescale. The specific definitions of these timescales will be clarified later.

beamformer using only its local CSI with respect to UTs, thereby eliminating the need for a centralized processor and complex inter-satellite coordination mechanisms.

This paper is structured as follows. We begin by presenting the system model in Section II. Section III examines both downlink positioning and uplink channel estimation performance through MCRB theory, incorporating the PACE. A distributed beamforming approach for downlink communications is detailed in Section IV. Numerical results are presented in Section V, with conclusions drawn in Section VII.

Notations: Scalars are written in regular lowercase, while vectors and matrices are denoted by bold lowercase and bold uppercase letters, respectively. For a vector \mathbf{a} , its 2-norm is expressed as $\|\mathbf{a}\|$. We use T and H as superscripts to indicate transpose and Hermitian transpose operations. For a matrix \mathbf{A} , $\text{Tr}(\mathbf{A})$ represents its trace. Complex numbers are handled by $\Re\{a\}$ and $\Im\{a\}$ for their real and imaginary components. A block-diagonal matrix constructed from matrices $\mathbf{A}_1, \dots, \mathbf{A}_N$ is written as $\text{blkdiag}\{\mathbf{A}_1, \dots, \mathbf{A}_N\}$. The Kronecker product is symbolized by \otimes . For statistical distributions, $\mathcal{CN}(\boldsymbol{\mu}, \mathbf{C})$ represents a circularly symmetric complex Gaussian distribution characterized by mean $\boldsymbol{\mu}$ and covariance matrix \mathbf{C} .

II. SYSTEM MODEL

As illustrated in Fig. 1, we consider a scenario where a cluster of S LEO satellites serves U UTs, simultaneously providing downlink positioning and communication services. Each LEO satellite is equipped with a UPA comprising $N = N_h \times N_v$ half-wavelength-spaced antennas, where N_h and N_v denote the numbers of antennas in the horizontal and vertical dimensions, respectively. Each UT is equipped with a single antenna. While accurate CSI is essential for achieving efficient downlink communication, channel estimation is challenging in space-borne communication systems due to the limited link

budget and short coherence time. These challenges originate from the long travel distance between the satellites and the UTs as well as the high-speed satellite movement [7]. In the following, we first introduce the adopted channel model. Subsequently, we elaborate on a two-timescale property of this model, which can be leveraged to facilitate efficient channel acquisition at LEO satellites, thereby enhancing downlink communications.

A. Channel Model

We consider a satellite communication system operating at relatively high-frequency bands such as the Ku and Ka bands, where the channel is dominated by LOS propagation [9], [13].¹ Assume the system employs the orthogonal frequency division multiplexing (OFDM) scheme with K subcarriers. Let $\Delta f = B/K$ and $T = 1/B$ denote the subcarrier spacing and symbol duration, respectively, where B is the signal bandwidth. The channel from the s -th LEO satellite to the u -th UT during the ℓ -th symbol over the k -th subcarrier is expressed as²

$$\mathbf{h}_{s,u}[\ell, k] = \alpha_{s,u} G(\boldsymbol{\theta}_{s,u}^{\text{el}}) e^{j2\pi(\ell T v_{s,u} - k \Delta f \tau_{s,u})} \mathbf{a}(\boldsymbol{\theta}_{s,u}), \quad (1)$$

where $\alpha_{s,u}$ is the complex channel gain, $G(\cdot)$ is the antenna radiation gain determined solely by the elevation angle [28], $\tau_{s,u}$ and $v_{s,u}$ represent the TOA and Doppler shift, respectively, and $\mathbf{a}(\boldsymbol{\theta}_{s,u}) \in \mathbb{C}^N$ is the steering vector at the LEO satellite, with $\boldsymbol{\theta}_{s,u} = [\theta_{s,u}^{\text{az}}, \theta_{s,u}^{\text{el}}]^{\text{T}}$ being the angle-of-departure (AOD) composed of both azimuth and elevation angles. Without loss of generality, we assume the UPA at each satellite is deployed

¹While the multipath effect can still play a significant role in dense urban environments, LEO satellite communications are primarily designed to serve suburban, rural, and remote areas, such as oceans and deserts, where terrestrial infrastructure is sparse or nonexistent, and scatterers are greatly reduced. Consequently, LOS propagation becomes even more dominant.

²Note that, though not further indexed for symbolic simplicity, this expression is viewed within one channel-gain coherent interval (as elaborated later) and $v_{s,u}$, $\tau_{s,u}$, and $\boldsymbol{\theta}_{s,u}$ are viewed constant for many such intervals.

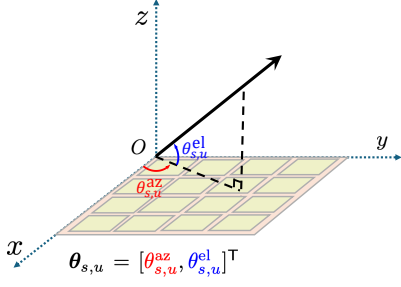


Fig. 2. Geometric configuration of the local coordinate systems for LEO satellites, depicting the UPA deployment in the XY-plane.

on the XY-plane of its local coordinate system, as illustrated in Fig. 2. Hence, the steering vector can be expressed as

$$\mathbf{a}(\boldsymbol{\theta}_{s,u}) = e^{-j2\pi\phi_{s,u}^h \mathbf{n}(N_h)} \otimes e^{-j2\pi\phi_{s,u}^v \mathbf{n}(N_v)}, \quad (2)$$

where $\mathbf{n}(N) = [0, \dots, N-1]^T$, $\phi_{s,u}^h = d \cos \theta_{s,u}^{\text{az}} \cos \theta_{s,u}^{\text{el}} / \lambda$, and $\phi_{s,u}^v = d \sin \theta_{s,u}^{\text{az}} \cos \theta_{s,u}^{\text{el}} / \lambda$. Here, d denotes the antenna spacing along each dimension, and λ is the wavelength at the central carrier frequency f_c .

The complex channel gain can be modeled as

$$\alpha_{s,u} = e^{j\psi_{s,u}} \beta_{s,u}, \quad (3)$$

where $\psi_{s,u}$ represents the random phase difference between the transmitter and receiver [29], and $\beta_{s,u}$ denotes the path loss incorporating both the large-scale path losses and small-scale fading, as described in [30]. Specifically, the path loss $\beta_{s,u}$, in the dB domain, is characterized as

$$-10 \log_{10} \beta_{s,u} = \beta_{s,u}^{\text{FS}} + \beta_{s,u}^{\text{SF}} + \beta_{s,u}^{\text{CL}} + \beta_{s,u}^{\text{AB}} + \beta_{s,u}^{\text{SC}} \text{ [dB]}, \quad (4)$$

where $\beta_{s,u}^{\text{FS}}$ denotes the free-space path loss, $\beta_{s,u}^{\text{SF}}$ accounts for shadow fading modeled as a Gaussian random variable, $\beta_{s,u}^{\text{CL}}$ represents the clutter loss, $\beta_{s,u}^{\text{AB}}$ captures atmospheric absorption effects, and $\beta_{s,u}^{\text{SC}}$ accounts for attenuation caused by ionospheric or tropospheric scintillation.

B. Timescale Analysis and Frame Structure

1) *Timescale Analysis*: From (1), we observe that the LEO satellite channel is governed by two categories of parameters:

- *Large-Timescale Parameters*: These parameters are associated with the UT's position, including the Doppler shift, TOA, and AOD. Due to the large geographical scale of satellite communications, they typically change slowly (on timescales of seconds) or can be accurately predicted through tracking mechanisms to reduce estimation overhead [25]. Although LEO satellites move rapidly, their orbits are typically predictable and well-determined. Therefore, while these parameters are related to the fast-varying position of LEO satellites, they can still be considered slow-varying due to their predictability.
- *Small-Timescale Parameters*: These parameters consist of random variations in the amplitude and phase of the channel gain. In contrast to the slow-varying parameters determined by geometry, these parameters are inherently unpredictable and fluctuate rapidly. For instance, tropospheric scintillation can cause phase and amplitude variations in Ka-band LEO satellite channels that fluctuate

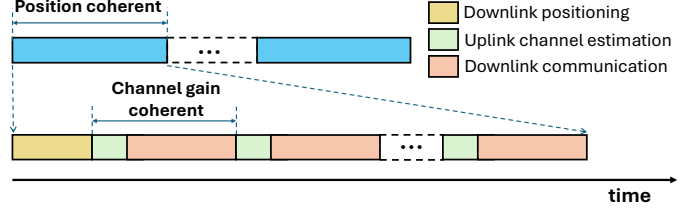


Fig. 3. Illustration of the two-timescale frame structure, where each large-timescale frame encompasses multiple small-timescale subframes. The large-timescale frame is governed by the position-coherent time, while the small-timescale subframe is defined by the channel gain-coherent time.

on sub-second timescales, with the exact rate depending on atmospheric and orbital conditions [31].

Notably, the Doppler shift caused by the high-speed movement of the satellite induces rapid temporal phase rotation in the channel. However, this effect can be largely mitigated through carrier synchronization at the receiver, albeit with minor residual errors [3]. As a result, its impact on LEO satellite communications is limited. Nonetheless, we retain it in the channel model because it can serve as a valuable measurement for positioning, as will be discussed later. For positioning purposes, the Doppler shift should be explicitly estimated before being compensated for communications.

2) *Two-Timescale Frame Structure*: Inspired by the timescale analysis, we propose a two-timescale frame structure that exploits the inherent two-timescale property of LEO channels to enable efficient channel estimation/reconstruction, thus facilitating downlink LEO transmission. As shown in Fig. 3, the duration of a large-timescale frame is determined by the position-coherent time, which indicates the interval after which the UTs' position information becomes outdated. Each large-timescale frame begins with an initial subframe for downlink positioning (where position estimates obtained by UTs are fed back to LEO satellites), followed by multiple small-timescale subframes during which the channel gain remains coherent. Each small-timescale subframe is further divided into slots for uplink channel estimation and downlink communication. Note that time division duplex (TDD) is adopted to differentiate between uplink and downlink transmissions. The proposed approach leverages uplink-downlink channel reciprocity, which applies uplink channel estimation to optimize downlink communication design.

To further substantiate the fundamental rationales behind the proposed structure for LEO downlink communications, we highlight its potential advantages by comparing it with positioning-free uplink channel estimation protocols, where the channel is directly estimated at the LEO satellites using uplink pilots without requiring position information from UTs [6], [8]. This approach involves estimating an unknown channel vector/matrix, which can incur significant pilot overhead, especially when large antenna arrays are employed. With the proposed position information-aided framework, vector-type channel estimation can be transformed into scalar-type estimation by exploiting the channel structure. This transformation offers the potential for higher channel estimation accuracy

with the same pilot overhead. Alternatively, to achieve equivalent channel estimation accuracy, reduced pilot overhead is required, thus preserving more resources for data transmission.

In the following, we will first conduct a performance analysis based on the two-timescale PACE and then propose a distributed beamforming method across multiple LEO satellites for downlink communication.

III. TWO-TIMESCALE POSITIONING-AIDED CHANNEL ESTIMATION

To characterize the performance limits of the proposed two-timescale PACE, we conduct a two-phase theoretical performance analysis. In the first phase, we analyze the downlink multi-LEO satellite-based positioning performance, while in the second phase, we assess the uplink channel estimation performance.

Before analyzing positioning performance, we acknowledge the presence of model mismatches due to hardware imperfections. First, low-cost oscillators and inherent hardware defects can introduce phase and frequency errors [32]. Second, clock biases are inevitable between satellites and UTs as well as between satellites themselves. Although a sub-nanosecond clock synchronization can be achieved by deploying GNSS receivers on LEO satellites [33], actual satellite signals remain subject to ionospheric and tropospheric delays during propagation [34]. These delays, influenced by factors such as temperature, pressure, humidity, and the satellite's elevation angle relative to the UT, result in unique delays for each satellite-UT pair, effectively introducing an additional clock bias in the signal model. Despite these non-idealities, many localization algorithms simplify the model by ignoring such factors to reduce computational complexity. For instance, in the scenario considered here, the large beam footprint of LEO satellite communication systems relaxes UT positioning accuracy requirements, while rapid channel variations prioritize model simplicity for timely estimations. Accordingly, we adopt a simplified model to estimate unknowns derived from a more complex realistic model, which inherently leads to model mismatches. Similarly, in the second phase, namely position information-aided channel estimation, the presence of estimation errors in UT positions also introduces model mismatches. Consequently, the performance bound under these model mismatches can be effectively analyzed using the tool of MCRB [27].

A. MCRB Basics

This subsection briefly recaps the fundamentals of MCRB. For a parameter $\bar{\theta} \in \mathbb{R}^{M \times 1}$, the lower bound (LB) matrix of the mean squared error of a mismatched estimator is provided by [27]

$$\text{LBM}(\tilde{\theta}) = \underbrace{\mathbf{A}_{\tilde{\theta}}^{-1} \mathbf{B}_{\tilde{\theta}} \mathbf{A}_{\tilde{\theta}}^{-1}}_{\text{MCRB}(\tilde{\theta})} + \underbrace{(\bar{\theta} - \tilde{\theta}) (\bar{\theta} - \tilde{\theta})^T}_{\text{Bias}(\tilde{\theta})}. \quad (5)$$

Here, $\tilde{\theta}$ denotes the pseudo-true parameter obtained by

$$\tilde{\theta} = \arg \min_{\theta} \mathcal{D} \{ \xi_{\mathcal{T}}(\mathbf{y}; \theta) \parallel \xi_{\mathcal{M}}(\mathbf{y}; \theta) \}, \quad (6)$$

where $\mathcal{D} \{ \xi_{\mathcal{T}}(\mathbf{y}; \theta) \parallel \xi_{\mathcal{M}}(\mathbf{y}; \tilde{\theta}) \}$ denotes the Kullback-Leibler (KL) divergence between the true likelihood function $\xi_{\mathcal{T}}(\mathbf{y}; \theta)$ and the mismatched likelihood function $\xi_{\mathcal{M}}(\mathbf{y}; \tilde{\theta})$. In addition, $\mathbf{A}_{\tilde{\theta}}$ and $\mathbf{B}_{\tilde{\theta}}$ represent two generalized Fisher information matrixs (FIMs), whose elements in the i -th row and the j -th column are determined by [27]

$$\begin{aligned} [\mathbf{A}_{\tilde{\theta}}]_{i,j} &= \mathbb{E}_{f_{\mathcal{T}}} \left\{ \left. \frac{\partial^2 \ln \xi_{\mathcal{M}}(\mathbf{y}; \theta)}{\partial [\theta]_i \partial [\theta]_j} \right|_{\theta=\tilde{\theta}} \right\} \\ &= 2\Re \left\{ \left(\frac{\partial^2 \boldsymbol{\mu}(\theta)}{\partial [\theta]_i \partial [\theta]_j} \right)^H \mathbf{C}_{\mathcal{M}}^{-1} \boldsymbol{\epsilon}(\theta) \right. \\ &\quad \left. - \left(\frac{\partial \boldsymbol{\mu}(\theta)}{\partial [\theta]_i} \right)^H \mathbf{C}_{\mathcal{M}}^{-1} \left(\frac{\partial \boldsymbol{\mu}(\theta)}{\partial [\theta]_j} \right) \right\} \Big|_{\theta=\tilde{\theta}}, \end{aligned} \quad (7)$$

and

$$\begin{aligned} [\mathbf{B}_{\tilde{\theta}}]_{i,j} &= \mathbb{E}_{f_{\mathcal{T}}} \left\{ \left. \frac{\partial \ln f_{\mathcal{M}}(\mathbf{y}; \theta)}{\partial [\theta]_i} \right|_{\theta=\tilde{\theta}} \frac{\partial \ln f_{\mathcal{M}}(\mathbf{y}; \theta)}{\partial [\theta]_j} \right|_{\theta=\tilde{\theta}} \right\} \\ &= 4\Re \left\{ \boldsymbol{\epsilon}(\theta)^H \mathbf{C}_{\mathcal{M}}^{-1} \frac{\partial \boldsymbol{\mu}(\theta)}{\partial [\theta]_i} \right\} \Re \left\{ \boldsymbol{\epsilon}(\theta)^H \mathbf{C}_{\mathcal{M}}^{-1} \frac{\partial \boldsymbol{\mu}(\theta)}{\partial [\theta]_j} \right\} \\ &\quad + 2\Re \left\{ \left(\frac{\partial \boldsymbol{\mu}(\theta)}{\partial [\theta]_i} \right)^H \mathbf{C}_{\mathcal{M}}^{-1} \left(\frac{\partial \boldsymbol{\mu}(\theta)}{\partial [\theta]_j} \right) \right\} \Big|_{\theta=\tilde{\theta}}, \end{aligned} \quad (8)$$

respectively. Here, $\mathbf{C}_{\mathcal{M}}$ represents the covariance matrix of $\xi_{\mathcal{M}}(\mathbf{y}; \theta)$ and $\boldsymbol{\epsilon}(\tilde{\theta}) = \boldsymbol{\kappa}(\tilde{\theta}) - \boldsymbol{\mu}(\tilde{\theta})$ with $\boldsymbol{\kappa}(\tilde{\theta})$ and $\boldsymbol{\mu}(\tilde{\theta})$ being the noise-free observations under the true and mismatched models, respectively [27], [35].

B. Large-Timescale Downlink Positioning

1) *Signal Model*: Let $\mathbf{t}_s[\ell, k] \in \mathbb{C}^U$ be the pilot (with unit-modulus elements) sent by the s -th LEO satellite over the ℓ -th symbol and the k -th subcarrier. We assume the satellites are multiplexed in the positioning phase through time-division multiple access (TDMA) [25]. The received baseband signal at the u -th user, from the s -th satellite can be expressed as

$$\begin{aligned} y_{s,u}[\ell, k] &= \mathbf{h}_{s,u}^T[\ell, k] \mathbf{F}_s \mathbf{t}_s[\ell, k] + z_u[\ell, k] \\ &= \alpha_{s,u} \gamma_{\theta_{s,u}^{\text{el}}}[\ell, k] \mathbf{a}^T(\boldsymbol{\theta}_{s,u}) \mathbf{f}_s[\ell, k] + z_u[\ell, k], \end{aligned} \quad (9)$$

where $\gamma_{\theta_{s,u}^{\text{el}}}[\ell, k] = G(\theta_{s,u}^{\text{el}}) e^{j2\pi(\ell T v_{s,u} - k \Delta f \tau_{s,u})}$, $\mathbf{f}_s[\ell, k] = \mathbf{F}_s \mathbf{t}_s[\ell, k]$ with $\mathbf{F}_s \in \mathbb{C}^{N \times U}$ being the beamforming matrix, and $z_u[\ell, k] \sim \mathcal{CN}(\mathbf{0}, N_0 \Delta f)$ is the additive white Gaussian noise (AWGN) with single-side power spectral density (PSD) N_0 . Without loss of generality, the following derivation focuses on the u -th user.

Let $\boldsymbol{\eta}_{s,u} = [\hat{\boldsymbol{\eta}}_{s,u}^T, \hat{\boldsymbol{\eta}}_{s,u}^T]^T \in \mathbb{R}^6$ be the unknown channel-domain parameters in signals received from the s -th satellite, where $\hat{\boldsymbol{\eta}}_{s,u} = [v_{s,u}, \tau_{s,u}]^T \in \mathbb{R}^2$ contains the channel-domain parameters we used to localize the user and $\hat{\boldsymbol{\eta}}_{s,u} = [\boldsymbol{\theta}_{s,u}^T, \Re(\alpha_{s,u}), \Im(\alpha_{s,u})]^T \in \mathbb{R}^4$ contains the other nuisance parameters that we do not explore. Note here the AOD $\boldsymbol{\theta}_{s,u}$ is unused for UT positioning due to the limited angular resolution of satellites. We further concatenate all the utilized channel-domain parameters collected from S satellites as $\hat{\boldsymbol{\eta}}_u = [\hat{\boldsymbol{\eta}}_{1,u}^T, \dots, \hat{\boldsymbol{\eta}}_{S,u}^T]^T \in \mathbb{R}^{2S}$. Therefore, in the large-timescale downlink positioning, we first estimate $\hat{\boldsymbol{\eta}}_u$ based

on $y_{s,u}[\ell, k]$, $s = 1, \dots, S$, $\ell = 1, \dots, L_p$, $k = 1, \dots, K$, where L_p denotes the number of pilot symbols for downlink positioning. Afterwards, we estimate the u -th user's position, clock biases, and CFOs.

2) *The FIM of $\eta_{s,u}$* : Let $\mu_{s,u}[\ell, k]$ denote the noise-free version of $y_{s,u}[\ell, k]$ and $\mathbf{G}_{s,u}[\ell, k] = [\mathbf{g}_v[\ell, k], \mathbf{g}_\tau[\ell, k], \mathbf{g}_{\theta_{az}}[\ell, k], \mathbf{g}_{\theta_{el}}[\ell, k], \mathbf{g}_{\alpha,R}[\ell, k], \mathbf{g}_{\alpha,I}[\ell, k]] \in \mathbb{C}^{N \times 6}$. Here, the columns fulfill

$$\mathbf{g}_v[\ell, k] = \alpha_{s,u} \gamma_{\theta_{s,u}^{el}}[\ell, k] (j2\pi\ell T) \mathbf{a}(\boldsymbol{\theta}_{s,u}), \quad (10a)$$

$$\mathbf{g}_\tau[\ell, k] = \alpha_{s,u} \gamma_{\theta_{s,u}^{el}}[\ell, k] (-j2\pi k \Delta f) \mathbf{a}(\boldsymbol{\theta}_{s,u}), \quad (10b)$$

$$\mathbf{g}_{\theta_{az}}[\ell, k] = \alpha_{s,u} \gamma_{\theta_{s,u}^{el}}[\ell, k] \frac{\partial \mathbf{a}(\boldsymbol{\theta}_{s,u})}{\partial \theta_{az}}, \quad (10c)$$

$$\mathbf{g}_{\theta_{el}}[\ell, k] = \alpha_{s,u} \left(\frac{\partial \gamma_{\theta_{s,u}^{el}}[\ell, k]}{\partial \theta_{s,u}^{el}} \mathbf{a}(\boldsymbol{\theta}_{s,u}) + \gamma_{\theta_{s,u}^{el}}[\ell, k] \frac{\partial \mathbf{a}(\boldsymbol{\theta}_{s,u})}{\partial \theta_{s,u}^{el}} \right), \quad (10d)$$

$$\mathbf{g}_{\alpha,R}[\ell, k] = \gamma_{\theta_{s,u}^{el}}[\ell, k] \mathbf{a}(\boldsymbol{\theta}_{s,u}), \quad (10e)$$

$$\mathbf{g}_{\alpha,I}[\ell, k] = j \gamma_{\theta_{s,u}^{el}}[\ell, k] \mathbf{a}(\boldsymbol{\theta}_{s,u}). \quad (10f)$$

Based on the signal received from the s -th satellite, the FIM of $\eta_{s,u}$ can be computed by the Slepian-Bangs formula as

$$\begin{aligned} & \mathbf{J}_s(\eta_{s,u}) \\ &= \frac{2}{N_0 \Delta f} \sum_{\ell=1}^{L_p} \sum_{k=1}^K \Re \left\{ \left(\frac{\partial \mu_{s,u}[\ell, k]}{\partial \eta_{s,u}} \right) \left(\frac{\partial \mu_{s,u}[\ell, k]}{\partial \eta_{s,u}} \right)^H \right\}, \quad (11) \\ &= \frac{2}{N_0 \Delta f} \sum_{\ell=1}^{L_p} \sum_{k=1}^K \Re \left\{ \mathbf{G}_{s,u}^T[\ell, k] \mathbf{f}_s[\ell, k] \mathbf{f}_s[\ell, k]^H \mathbf{G}_{s,u}^*[\ell, k] \right\}. \end{aligned}$$

3) *The FIM of $\hat{\eta}_u$* : Partitioning $\mathbf{J}_s(\eta_{s,u}) = [\mathbf{X}, \mathbf{Y}; \mathbf{Y}^T, \mathbf{Z}]$, where $\mathbf{X} \in \mathbb{R}^{2 \times 2}$, we can compute the FIM of the total utilized channel-domain parameters $\hat{\eta}_{s,u}$ as $\mathbf{J}_s(\hat{\eta}_{s,u}) = \mathbf{X} - \mathbf{Y}\mathbf{Z}^{-1}\mathbf{Y}^T$. Then, we can obtain the FIM of $\hat{\eta}_u$ as

$$\mathbf{J}(\hat{\eta}_u) = \text{blkdiag}\{\mathbf{J}_1(\hat{\eta}_{1,u}), \dots, \mathbf{J}_S(\hat{\eta}_{S,u})\}. \quad (12)$$

Based on this, we can infer that the achievable lowest estimation error on $\hat{\eta}_u$ regardless of the adopted algorithms is characterized by the Gaussian distribution $\mathcal{N}(\mathbf{0}, \mathbf{J}_s^{-1}(\hat{\eta}_u))$. Any algorithm achieving this error covariance matrix is called an *efficient estimator*.

4) *MCRB and LB Derivation*: Suppose an efficient estimator is utilized to estimate $\hat{\eta}_u$. We now focus on estimating the position-domain parameters, where the aforementioned model mismatches occur. We consider a scenario where each satellite-UT pair has a distinct clock bias $b_{s,u}$ and CFO $\delta_{s,u}$. For convenience, we use b_u and δ_u to denote an average clock bias and CFO among the S satellites, thus we can rewrite these individual clock biases and CFOs as $b_{s,u} = b_u + \Delta b_{s,u}$ and $\delta_{s,u} = \delta_u + \Delta \delta_{s,u}$, respectively, where $\Delta b_{s,u}$ and $\Delta \delta_{s,u}$ denote the differences on each clock bias and CFO.

Let $\mathbf{v}_s \in \mathbb{R}^3$ be the velocity of the s -th LEO satellite. Here, as the velocity of LEO satellite is usually much higher than that of the UT, we ignore the velocity contribution from the UT side. Based on the underlying geometric relationship, the forward model between the entries of $\hat{\eta}_u$ and unknown

position of the u -th user can be expressed as

$$v_{s,u} = \frac{\mathbf{v}_s^T (\mathbf{p}_u - \mathbf{p}_s)}{\lambda \|\mathbf{p}_u - \mathbf{p}_s\|} + \delta_u + \Delta \delta_{s,u}, \quad (13a)$$

$$\tau_{s,u} = \frac{\|\mathbf{p}_u - \mathbf{p}_s\|}{c} + b_u + \Delta b_{s,u}, \quad (13b)$$

which we refer to as the *true model*. In real applications, we often ignore these clock bias and CFO differences, i.e., assuming all satellite-UT pairs have the same clock bias and CFO, for algorithmic simplicity. To account for the impact of such model mismatch, here we derive the MCRB. When neglecting the difference on each clock bias and CFO, the *mismatched model* is given by

$$v_{s,u} = \frac{\mathbf{v}_s^T (\mathbf{p}_u - \mathbf{p}_s)}{\lambda \|\mathbf{p}_u - \mathbf{p}_s\|} + \delta_u, \quad (14a)$$

$$\tau_{s,u} = \frac{\|\mathbf{p}_u - \mathbf{p}_s\|}{c} + b_u. \quad (14b)$$

Now, we suppose a mismatched estimator that aims to estimate the unknown position of the u -th user based on the realistic observation $\hat{\eta}_u$ and simplified model (14). The total unknown parameters in the mismatch model can be concatenated as $\mathbf{r}_u = [\mathbf{p}_u^T, \delta_u, b_u]^T \in \mathbb{R}^5$. Based on the true model (13) and mismatched model (14), we can respectively express the true likelihood function ξ_T and the mismatched likelihood function ξ_M as

$$\ln \xi_T(\hat{\eta}_u; \mathbf{r}_u) \propto (\hat{\eta}_u - \bar{\mathbf{f}}(\mathbf{r}_u))^T \boldsymbol{\Sigma}^{-1} (\hat{\eta}_u - \bar{\mathbf{f}}(\mathbf{r}_u)), \quad (15)$$

and

$$\ln \xi_M(\hat{\eta}_u; \mathbf{r}_u) \propto (\hat{\eta}_u - \tilde{\mathbf{f}}(\mathbf{r}_u))^T \boldsymbol{\Sigma}^{-1} (\hat{\eta}_u - \tilde{\mathbf{f}}(\mathbf{r}_u)), \quad (16)$$

respectively, where the function $\bar{\mathbf{f}}(\cdot)$ maps \mathbf{r}_u to $\hat{\eta}_u$ according to (13), and the function $\tilde{\mathbf{f}}(\cdot)$ maps \mathbf{r}_u to $\hat{\eta}_u$ according to (14). As mentioned in Section III-B3, $\hat{\eta}_u$ is the estimated channel-domain parameters through an efficient estimator, i.e., $\hat{\eta}_u \sim \mathcal{N}(\bar{\mathbf{f}}(\mathbf{r}_u), \boldsymbol{\Sigma})$, where $\boldsymbol{\Sigma} = \mathbf{J}^{-1}(\hat{\eta}_u)$.

- *Pseudo-True Parameter*: According to (6), the pseudo-true parameter, denoted by $\tilde{\mathbf{r}}_u$, is given by

$$\tilde{\mathbf{r}}_u = \arg \min_{\mathbf{r}_u} \mathcal{D} \{ \xi_T(\hat{\eta}_u; \tilde{\mathbf{r}}_u) \mid \xi_M(\hat{\eta}_u; \mathbf{r}_u) \}, \quad (17)$$

= $\arg \min_{\mathbf{r}_u} (\bar{\mathbf{f}}(\tilde{\mathbf{r}}_u) - \tilde{\mathbf{f}}(\mathbf{r}_u))^T \boldsymbol{\Sigma}^{-1} (\bar{\mathbf{f}}(\tilde{\mathbf{r}}_u) - \tilde{\mathbf{f}}(\mathbf{r}_u))$, where the top bar is used to highlight the ground-truth position-domain parameter and forward model. The above problem can be solved using gradient descent with backtracking line search, wherein the true parameters serve as the initial point [35].

- *MCRB*: According to (7) and (8), the generalized FIMs, i.e., $\mathbf{A}_{\tilde{\mathbf{r}}_u}$ and $\mathbf{B}_{\tilde{\mathbf{r}}_u}$, can be computed by determining the first- and second-order derivatives of $\tilde{\mathbf{f}}(\mathbf{r}_u)$ with respect to the elements of \mathbf{r}_u , as detailed in Appendix A. Subsequently, the MCRB is expressed as

$$\text{MCRB}(\tilde{\mathbf{r}}_u) = \mathbf{A}_{\tilde{\mathbf{r}}_u}^{-1} \mathbf{B}_{\tilde{\mathbf{r}}_u} \mathbf{A}_{\tilde{\mathbf{r}}_u}^{-1}. \quad (18)$$

- *LB*: Finally, the estimation error LB matrix can be computed according to (5) as

$$\text{LBM}(\tilde{\mathbf{r}}_u) = \text{MCRB}(\tilde{\mathbf{r}}_u) + \text{Bias}(\tilde{\mathbf{r}}_u), \quad (19)$$

where $\text{Bias}(\tilde{\mathbf{r}}_u) = (\bar{\mathbf{r}}_u - \tilde{\mathbf{r}}_u) (\bar{\mathbf{r}}_u - \tilde{\mathbf{r}}_u)^T$. Based on (19), the LB for the expected root mean squared error (RMSE) of the u -th UT's position estimation in the presence of

model mismatch is given by

$$\text{LB}(\mathbf{p}_u) = \sqrt{\text{Tr}([\text{LBM}(\tilde{\mathbf{r}}_u)]_{1:3,1:3})}. \quad (20)$$

C. Small-Timescale Uplink Channel Estimation

1) *Signal Model*: After obtaining the positions of UTs, these large-timescale parameters are fed back to the LEO satellites. The second phase of PACE then focuses on estimating the small-timescale parameters (i.e., the channel gains) at the LEO satellites through uplink channel estimation, followed by complete channel reconstruction.

Let $\mathbf{d}_{s,u}[\ell, k] = \mathbf{a}(\boldsymbol{\theta}_{s,u})\sqrt{P_u/K}t_u[\ell, k]$, where P_u denotes the transmit power of the u -th UT, and $t_u[\ell, k]$ represents the unit-modulus pilot transmitted by the u -th UT during the ℓ -th symbol and the k -th subcarrier. Uniform power allocation is employed across all subcarriers. As previously mentioned, the Doppler shift can be largely mitigated in LEO satellite communications. After being exploited in downlink positioning, it is excluded from the signal model including uplink channel estimation and downlink communication for simplicity. Here, we also assume UTs are multiplexed orthogonally using TDMA. By channel reciprocity, the signal received by the s -th LEO satellite from the u -th UT is expressed as

$$\mathbf{y}_{s,u}[\ell, k] = \underbrace{\vartheta_{s,u}e^{-j2\pi k\Delta f\tau_{s,u}}\mathbf{d}_{s,u}[\ell, k]}_{\tilde{\mathbf{g}}_{s,u}[\ell, k]} + \mathbf{z}_s[\ell, k], \quad (21)$$

where $\vartheta_{s,u} = \alpha_{s,u}G(\theta_{s,u}^{\text{el}})$ and $\mathbf{z}_s[\ell, k] \sim \mathcal{CN}(\mathbf{0}, N_0\Delta f\mathbf{I}_N)$ represents the AWGN.

We observe that $\mathbf{d}_{s,u}[\ell, k]$ is directly determined by the UTs' position feedback. Consequently, instead of estimating the full channel vector, it suffices to estimate only two scalars, i.e., the channel gain $\vartheta_{s,u}$ and the TOA $\tau_{s,u}$. This significantly simplifies the uplink channel estimation task. However, since the position information is based on estimation rather than ground truth, model mismatch arises again. The received signal based on the estimated position information (mismatched model) is expressed as

$$\mathbf{y}_{s,u}[\ell, k] = \underbrace{\vartheta_{s,u}e^{-j2\pi k\Delta f\tau_{s,u}}\tilde{\mathbf{d}}_{s,u}[\ell, k]}_{\tilde{\mathbf{g}}_{s,u}[\ell, k]} + \mathbf{z}_s[\ell, k], \quad (22)$$

where $\tilde{\mathbf{d}}_{s,u}[\ell, k] = \mathbf{a}(\tilde{\boldsymbol{\theta}}_{s,u})\sqrt{P_u/K}t_u[\ell, k]$. Here, $\tilde{\boldsymbol{\theta}}_{s,u}$ represents the calculated angle-of-arrival (AOA) based on the estimated $\tilde{\mathbf{p}}_u$ and the geometrical relationship, given by

$$\tilde{\theta}_{s,u}^{\text{az}} = \text{atan2}([\tilde{\mathbf{p}}_u - \mathbf{p}_s]_2, [\tilde{\mathbf{p}}_u - \mathbf{p}_s]_1), \quad (23a)$$

$$\tilde{\theta}_{s,u}^{\text{el}} = \text{asin}\left(\frac{([\tilde{\mathbf{p}}_u - \mathbf{p}_s]_3)}{\|\tilde{\mathbf{p}}_u - \mathbf{p}_s\|}\right). \quad (23b)$$

2) *MCRB and LB Derivation*: We denote the total temporal and spectral observation as $\mathbf{y}_{s,u} = [\mathbf{y}_{s,u}^T[1, 1], \dots, \mathbf{y}_{s,u}^T[1, K], \dots, \mathbf{y}_{s,u}^T[L_c, K]]^T \in \mathbb{C}^{L_cKN}$, where L_c represents the number of pilot symbols used for uplink channel estimation. Let $\boldsymbol{\eta}_{s,u} = [\Re(\vartheta_{s,u}), \Im(\vartheta_{s,u}), \tau_{s,u}]^T \in \mathbb{R}^3$ collect the parameters to be estimated in the uplink channel estimation. The likelihood functions under the true and mismatched models are given by

$$\ln \xi_{\text{T}}(\mathbf{y}_{s,u}; \boldsymbol{\eta}_{s,u}) \propto \|\mathbf{y}_{s,u} - \tilde{\mathbf{g}}(\boldsymbol{\eta}_{s,u})\|^2, \quad (24)$$

and

$$\ln \xi_{\text{M}}(\mathbf{y}_{s,u}; \boldsymbol{\eta}_{s,u}) \propto \|\mathbf{y}_{s,u} - \tilde{\mathbf{g}}(\boldsymbol{\eta}_{s,u})\|^2, \quad (25)$$

respectively, where we define $\tilde{\mathbf{g}}(\boldsymbol{\eta}_{s,u}) = [\tilde{\mathbf{g}}_{s,u}^T[1, 1], \dots, \tilde{\mathbf{g}}_{s,u}^T[1, K], \dots, \tilde{\mathbf{g}}_{s,u}^T[L_c, K]]^T \in \mathbb{C}^{L_cKN}$ and $\tilde{\mathbf{g}}(\boldsymbol{\eta}_{s,u}) = [\tilde{\mathbf{g}}_{s,u}^T[1, 1], \dots, \tilde{\mathbf{g}}_{s,u}^T[1, K], \dots, \tilde{\mathbf{g}}_{s,u}^T[L_c, K]]^T \in \mathbb{C}^{L_cKN}$.

- *Pseudo-True Parameter*: According to (6), the pseudo-true parameter, denoted by $\tilde{\boldsymbol{\eta}}_{s,u}$, is derived as

$$\begin{aligned} \tilde{\boldsymbol{\eta}}_{s,u} &= \arg \min_{\boldsymbol{\eta}_{s,u}} \mathcal{D}\{\xi_{\text{T}}(\mathbf{y}_{s,u}; \boldsymbol{\eta}_{s,u}) \|\xi_{\text{M}}(\mathbf{y}_{s,u}; \boldsymbol{\eta}_{s,u})\}, \\ &= \arg \min_{\boldsymbol{\eta}_{s,u}} \|\bar{\mathbf{q}}(\tilde{\boldsymbol{\eta}}_{s,u}) - \bar{\mathbf{q}}(\boldsymbol{\eta}_{s,u})\|^2, \end{aligned} \quad (26)$$

where the bar above the parameter emphasizes the ground-truth value. Once again, by employing gradient descent and treating truth parameter as initial point, the above problem can be efficiently solved [35].

- *MCRB*: The generalized FIMs, i.e., $\mathbf{A}_{\tilde{\boldsymbol{\eta}}_{s,u}}$ and $\mathbf{B}_{\tilde{\boldsymbol{\eta}}_{s,u}}$, are obtained by calculating the first- and second-order derivatives of $\bar{\mathbf{q}}(\boldsymbol{\eta}_{s,u})$ with respect to the elements of $\boldsymbol{\eta}_{s,u}$, as described in Appendix B. Based on these, the MCRB is given by

$$\text{MCRB}(\tilde{\boldsymbol{\eta}}_{s,u}) = \mathbf{A}_{\tilde{\boldsymbol{\eta}}_{s,u}}^{-1} \mathbf{B}_{\tilde{\boldsymbol{\eta}}_{s,u}} \mathbf{A}_{\tilde{\boldsymbol{\eta}}_{s,u}}^{-1}. \quad (27)$$

- *LB*: The estimation error LB matrix is then calculated as

$$\text{LBM}(\tilde{\boldsymbol{\eta}}_{s,u}) = \text{MCRB}(\tilde{\boldsymbol{\eta}}_{s,u}) + \text{Bias}(\tilde{\boldsymbol{\eta}}_{s,u}), \quad (28)$$

where $\text{Bias}(\tilde{\boldsymbol{\eta}}_{s,u}) = (\tilde{\boldsymbol{\eta}}_{s,u} - \boldsymbol{\eta}_{s,u})(\tilde{\boldsymbol{\eta}}_{s,u} - \boldsymbol{\eta}_{s,u})^T$. For an efficient estimator, the LB for the expected RMSE of the channel gain $\vartheta_{s,u}$ and the TOA $\tau_{s,u}$, in the presence of model mismatch, are expressed as

$$\text{LB}(\vartheta_{s,u}) = \sqrt{\text{Tr}([\text{LBM}(\tilde{\boldsymbol{\eta}}_{s,u})]_{1:2,1:2})}, \quad (29)$$

and

$$\text{LB}(\tau_{s,u}) = \sqrt{[\text{LBM}(\tilde{\boldsymbol{\eta}}_{s,u})]_{3,3}}, \quad (30)$$

respectively.

IV. DISTRIBUTED BEAMFORMING FOR DOWNLINK COMMUNICATIONS

The proposed two-timescale PACE enables channel reconstruction between each LEO satellite and all UTs, enabling CSI-based beamforming for downlink communication. To address the limited link budget in single-satellite downlink scenarios, we introduce distributed multi-LEO satellite beamforming where each UT is served by the same satellite cluster. This distributed approach eliminates the need for inter-satellite CSI sharing, as beamforming decisions are made locally at each satellite using only its CSI, rather than requiring consolidated global CSI, which significantly reduces system complexity and latency.

A. Signal Model

Without centralized coordination, we manage inter-satellite interference by allocating orthogonal frequency bands to different LEO satellites. The total subcarrier set $\Phi = \{1, 2, \dots, K\}$ is partitioned into S equal subsets $\Phi_1, \Phi_2, \dots, \Phi_S$ corresponding to S LEO satellites. For each satellite s , its subset is defined as $\Phi_s = \{(s-1)K + 1, (s-$

$1)\bar{K} + 1, \dots, s\bar{K}\}$, where $\bar{K} = K/S$. For the s -th LEO satellite transmitting over the k -th subcarrier ($k \in \Phi_s$), the signal is given by

$$\mathbf{x}_s[k] = \mathbf{W}_s \mathbf{s}[k], \quad (31)$$

where $\mathbf{W}_s = [\mathbf{w}_{s,1}, \mathbf{w}_{s,2}, \dots, \mathbf{w}_{s,U}] \in \mathbb{C}^{N \times U}$ represents the beamformer³ for the s -th LEO satellite, and $\mathbf{s}[k] \sim \mathcal{CN}(\mathbf{0}, \mathbf{I}_U)$ denotes the data streams transmitted to U UTs over the k -th subcarrier.

The received signal at the u -th UT from the s -th LEO satellite over the k -th subcarrier can be represented as

$$y_u[k] = \mathbf{h}_{s,u}^\top[k] \mathbf{w}_{s,u} s_u[k] + \underbrace{\sum_{m=1, m \neq u}^U \mathbf{h}_{s,u}^\top[k] \mathbf{w}_{s,m} s_m[k]}_{\text{Inter-user interference}} + z_u[k], \quad (32)$$

where $\mathbf{h}_{s,u}[k] = \alpha_{s,u} G(\theta_{s,u}^{\text{e1}}) e^{-j2\pi k \Delta f \tau_{s,u}} \mathbf{a}(\theta_{s,u})$ denotes the channel vector incorporating Doppler shift compensation. The term $z_u[k] \sim \mathcal{CN}(\mathbf{0}, N_0 \Delta f)$ represents the AWGN. The achievable communication rate for the u -th UT, aggregated across all satellites and assigned subcarriers, is given by

$$R_u = \sum_{s=1}^S \sum_{k \in \Phi_s} R_{s,u}[k], \quad (33)$$

where $R_{s,u}[k]$ represents the communication rate between the s -th LEO satellite and the u -th UT over the k -th subcarrier, calculated as

$$R_{s,u}[k] = \log_2 \left(1 + \frac{|\mathbf{h}_{s,u}^\top[k] \mathbf{w}_{s,u}|^2}{I_{s,u}[k] + N_0 \Delta f} \right), \quad (34)$$

where $I_{s,u}[k] = \sum_{m=1, m \neq u}^U |\mathbf{h}_{s,u}^\top[k] \mathbf{w}_{s,m}|^2$.

B. Problem Formulation

We aim to optimize the beamformers at each LEO satellite to maximize the sum rate of all UTs. The optimization problem is formulated as follows

$$\begin{aligned} \max_{\mathbf{W}_s} \quad & \sum_{u=1}^U R_u = \sum_{u=1}^U \sum_{s=1}^S \sum_{k \in \Phi_s} R_{s,u}[k] \\ \text{s.t.} \quad & \sum_{u=1}^U \|\mathbf{w}_{s,u}\|^2 \leq \frac{P_s}{\bar{K}}, \quad \forall s, \end{aligned} \quad (35)$$

where P_s denotes the power budget at the s -th LEO satellite.

Note that, because $\sum_{u=1}^U \sum_{s=1}^S \sum_{k \in \Phi_s} R_{s,u}[k] = \sum_{s=1}^S \sum_{u=1}^U \sum_{k \in \Phi_s} R_{s,u}[k]$, the problem in (35) is inherently distributed. Consequently, a subproblem corresponding to the

³We adopt subcarrier-coherent beamforming, where the beamformer is consistent across subcarriers, with only amplitude adjustments allowed. This approach strikes a balance between performance and computational efficiency, which is critical given the limited onboard processing capabilities of LEO satellites. Although less flexible than subcarrier-specific beamforming, it substantially reduces optimization complexity in systems with a large number of subcarriers. The framework can be extended to subcarrier-specific beamforming, albeit at the expense of increased computational complexity.

s -th LEO satellite can be expressed as

$$\begin{aligned} \max_{\mathbf{W}_s} \quad & \sum_{u=1}^U \sum_{k \in \Phi_s} R_{s,u}[k] \\ \text{s.t.} \quad & \sum_{u=1}^U \|\mathbf{w}_{s,u}\|^2 \leq \frac{P_s}{\bar{K}}. \end{aligned} \quad (36)$$

By solving (36) for each LEO satellite, the original problem in (35) can be effectively addressed.

C. Proposed Distributed Beamforming Approach

In the following, we employ the weighted sum mean squared error minimization (WMMSE) optimization framework [36] to solve (36) iteratively. Specifically, by introducing the auxiliary variables $\mu_{s,u}[k]$ and $\omega_{s,u}[k]$, where $\mu_{s,u}[k]$ and $\omega_{s,u}[k]$ serve as the MMSE equalizer and weight, respectively [36], (36) can be equivalently reformulated as

$$\begin{aligned} \max_{\mu_{s,u}[k], \omega_{s,u}[k], \mathbf{W}_s} \quad & \sum_{u=1}^U \sum_{k \in \Phi_s} \log_2 \omega_{s,u}[k] - \omega_{s,u}[k] \Psi_{s,u}[k] \\ \text{s.t.} \quad & \sum_{u=1}^U \|\mathbf{w}_{s,u}\|^2 \leq \frac{P_s}{\bar{K}}, \end{aligned} \quad (37)$$

where $\Psi_{s,u}[k] = |1 - \mu_{s,u}[k] \mathbf{h}_{s,u}^\top[k] \mathbf{w}_{s,u}|^2 + |\mu_{s,u}[k]|^2 (I_{s,u}[k] + N_0 \Delta f)$. The optimization problem in (37) is solved by iteratively updating \mathbf{W}_s , $\omega_{s,u}[k]$, and $\mu_{s,u}[k]$, as detailed below.

1) *Update $\mu_{s,u}[k]$* : With $\omega_{s,u}[k]$ and \mathbf{W}_s fixed, the optimal $\mu_{s,u}[k]$ is derived by setting $\partial \Psi_{s,u}[k] / \partial \mu_{s,u}[k] = 0$, resulting in

$$\mu_{s,u}[k] = \frac{\mathbf{h}_{s,u}^\top[k] \mathbf{w}_{s,u}}{I_{s,u}[k] + N_0 \Delta f}. \quad (38)$$

2) *Update $\omega_{s,u}[k]$* : With $\mu_{s,u}[k]$ and \mathbf{W}_s fixed, the optimal $\omega_{s,u}[k]$ is obtained by setting $\partial \Psi_{s,u}[k] / \partial \omega_{s,u}[k] = 0$, leading to

$$\omega_{s,u}[k] = \frac{1}{\Psi_{s,u}[k]}. \quad (39)$$

3) *Update \mathbf{W}_s* : With $\mu_{s,u}[k]$ and $\omega_{s,u}[k]$ fixed, the optimization problem to find the optimal \mathbf{W}_s is formulated as

$$\begin{aligned} \min_{\mathbf{W}_s} \quad & \sum_{u=1}^U \sum_{k \in \Phi_s} \Psi_{s,u}[k] \\ \text{s.t.} \quad & \sum_{u=1}^U \|\mathbf{w}_{s,u}\|^2 \leq \frac{P_s}{\bar{K}}. \end{aligned} \quad (40)$$

Here, $\Psi_{s,u}[k]$ can be expressed as the sum of a positive semi-definite quadratic form and a linear term. Consequently, (40) is a convex quadratically constrained quadratic program (QCQP) problem with respect to \mathbf{W}_s , which can be efficiently solved via convex optimization toolboxes such as CVX.

The process of solving (35) is outlined in Algorithm 1. The initial beamformer \mathbf{W}_s for the s -th LEO satellite can be constructed using maximum ratio transmission (MRT), which aligns the beamformer with the reconstructed channels (by excluding the frequency-dependent delay-induced phase rotation). Specifically, we have $\mathbf{W}_s =$

Algorithm 1 Algorithm for Solving (35)

```

1: Initialize:  $\mathbf{W}_s, \forall s$ ;
2: for  $s = 1 : S$  do
3:   repeat
4:     Update  $\mu_{s,u}[k]$  using (38);
5:     Update  $\omega_{s,u}[k]$  using (39);
6:     Update  $\mathbf{W}_s$  by solving (40) via CVX;
7:   until the reduction ratio of the objective value falls
     below a predefined threshold;
8: end for
9: Output:  $\mathbf{W}_s, \forall s$ .

```

TABLE I
SIMULATION PARAMETERS

Parameter	Value
Central carrier frequency f_c	12.7 GHz (Ku band)
Subcarrier spacing Δf	120 KHz
Subcarrier number K	1024
Power budget at each LEO satellite	50 dBm
Power budget at each UT	30 dBm
PSD N_0	-173.855 dBm/Hz
Noise figure F	10 dB
Number of LEO satellites S	8
Number of UTs U	4
Antenna number $N = N_h \times N_v$	8×8
Antenna radiation gain $G(\cdot)$	$\cos(\cdot)$

$\zeta_s[\hat{\vartheta}_{s,1}^* \mathbf{a}^*(\hat{\theta}_{s,1}), \dots, \hat{\vartheta}_{s,U}^* \mathbf{a}^*(\hat{\theta}_{s,U})]$, where the hat notation indicates estimated values and ζ_s is a normalization factor that ensures the fulfillment of the power budget. Since the WMMSE optimization framework is utilized to solve each subproblem, i.e., (36), its convergence is well-established [36]. The computational complexity of each iteration is primarily determined by solving (40), which, due to its QCQP nature, is characterized by $\mathcal{O}(N^3U^3)$.

V. NUMERICAL RESULTS

A. Simulation Parameters

As shown in Fig. 4, we model Earth as a semi-sphere with radius $r_E = 6400$ km and establish a spherical coordinate system centered at Earth's core. The region of interest where UTs are distributed is bounded by a dotted circle defined by the inclination angle φ . Within this region, the positions of U user terminals, i.e., $\mathbf{p}_u, u = 1, \dots, U$, are uniformly distributed. The LEO satellite orbits at an altitude of $h_S = 500$ km, forming a larger semi-sphere with radius $r_S = r_E + h_S$. The positions of S satellites, i.e., $\mathbf{p}_s, s = 1, \dots, S$, are positioned above the terrestrial area in a configuration that ensures visibility to all UTs. Each satellite traverses an orbit perpendicular to the XY-plane and intersects the z axis. The satellites maintain a constant velocity of $\|\mathbf{v}_s\| = 7.6$ km/s, with velocity vectors \mathbf{v}_s tangential to their orbits. The UPA installed on each satellite is oriented tangentially to the orbit, with its local coordinate system's z axis pointing toward the Earth's core and its x axis perpendicular to the orbital plane. Due to imperfect time-domain and frequency-domain synchronization, the clock bias (respectively, CFO) between

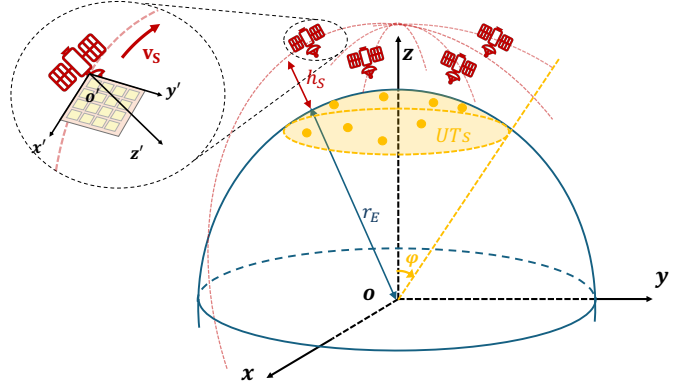


Fig. 4. Illustrative example of the considered scenario.

each satellite and the UT is randomly set to a value between 80 ns and 120 ns (respectively, between $\Delta f/120$ and $\Delta f/80$), which remains fixed throughout the simulation. To eliminate satellite handover involvement, we consider one large-timescale position-coherent frame containing 100 small-timescale channel gain-coherent subframes. Throughout this frame, the satellite constellation topology remains constant for simplicity. The downlink positioning consists of 1000 blocks, with each block having a duration of $10/\Delta f$. The uplink channel estimation utilizes $L_c = 1000$ pilots.

The channel gain from each LEO satellite to each UT, expressed by (3), is independently generated in each channel-gain coherent slot. The random phase $\psi_{s,u}$ is uniformly distributed in $[0, 2\pi]$. The components that constitute the path loss $\beta_{s,u}$ are generated according to (4). The free-space path loss is given by $\beta_{s,u}^{\text{FS}} = 20 \log_{10}(\|\mathbf{p}_u - \mathbf{p}_s\|) + 20 \log_{10}(f_c) - 145.55$ [dB] [30]. The atmospheric absorption $\beta_{s,u}^{\text{AB}}$, which depends on signal frequency and satellite elevation angle, is calculated according to International Telecommunication Union (ITU) recommendations [37] and configured using an off-the-shelf MATLAB script [38]. In the considered LOS-dominant suburban/rural/remote scenarios, the clutter loss $\beta_{s,u}^{\text{CL}}$ and the shadow fading $\beta_{s,u}^{\text{SF}}$ originating from near-surface structures are typically weak [39]. Therefore, we set $\beta_{s,u}^{\text{CL}} = 0$ dB and $\beta_{s,u}^{\text{SF}} = 0$ dB for convenience. Additionally, ionospheric scintillation can be ignored for frequencies above 6 GHz [30]. For $\beta_{s,u}^{\text{CL}}$ caused by tropospheric scintillation, which is generally difficult to model analytically, we adopt the example suggested in [25] as a reference value. The remaining simulation parameters are listed in Table I.

B. Compared Schemes

1) *Downlink Positioning:* Since we do not optimize the beamforming matrix \mathbf{F}_s , it is generated directly based on two principles, which differ depending on whether position information is utilized:

- **Position-Aided Beamforming (PAB):** Leveraging the position information of UTs obtained from the previous position-coherent frame, each LEO satellite constructs \mathbf{F}_s as a matrix whose columns correspond to the conjugates of the steering vectors for the UTs' estimated directions.

Specifically, $\mathbf{F}_s = \bar{\zeta}_s[\mathbf{a}^*(\hat{\theta}_{s,1}), \dots, \mathbf{a}^*(\hat{\theta}_{s,U})]$, where $\bar{\zeta}_s$ is a normalization factor that ensures compliance with the power budget.

- Vertically Directed Beamforming (VDB): In the absence of position information, each LEO satellite generates a vertical beam directed toward the Earth’s core. In this case, the beamforming matrix reduces to a steering vector with an elevation angle of $\pi/2$.

2) *Uplink Channel Estimation*: Depending on the availability of position information at the LEO satellites, we consider three types of schemes for evaluating the performance of uplink channel estimation:

- PACE: This is the proposed two-timescale hybrid downlink positioning and uplink channel estimation scheme. Its performance is rigorously characterized through MCRB analysis.
- Perfect-PACE: This represents an ideal benchmark where perfect position information of the UTs is assumed to be available at the LEO satellites. In this case, the performance of uplink channel estimation is evaluated without model mismatch and analyzed using the CRB.
- Uplink Channel Estimation (UCE): As previously discussed, in the absence of position information, the channel vector, i.e., $\mathbf{h}_{s,u}[k] = e^{-j2\pi k\Delta f\tau_{s,u}}\alpha_{s,u}G(\theta_{s,u}^{\text{el}})\mathbf{a}(\theta_{s,u})$, can be directly estimated in the uplink using a *geometry-agnostic* approach. By defining $\mathbf{h}_{s,u} = \alpha_{s,u}G(\theta_{s,u}^{\text{el}})\mathbf{a}(\theta_{s,u})$, we analyze the performance limits of estimating $\mathbf{h}_{s,u}$ and $\tau_{s,u}$ simultaneously by deriving the CRB. This derivation extends the approach in [40], which was originally developed for a single-carrier system.

3) *Downlink Communication*: To evaluate the performance of downlink communication, we utilize the CSI obtained through the different channel estimation schemes introduced above to perform distributed beamforming, as summarized in Algorithm 1. The resulting beamformer is tested using ground-truth CSI, yielding the actual sum rate. Additionally, we consider two alternative benchmarks:

- PAB: This approach is identical to the one introduced for downlink positioning, which relies solely on position information. However, the beamformer at each LEO satellite is applied only to a subset of subcarriers.
- Single-Satellite Service (S^3): In this method, each UT is served by only a single LEO satellite. Specifically, the one providing the strongest signal strength, rather than being served by all satellites within a cluster.

C. Downlink Positioning

As shown in Fig. 5, we compare the positioning error bounds and biases under PAB and VDB as functions of the per-satellite power budget. The results reveal that the LB of positioning error without model mismatch (represented by the positioning CRB under perfectly time- and frequency-synchronized satellites) decreases with increasing power. In

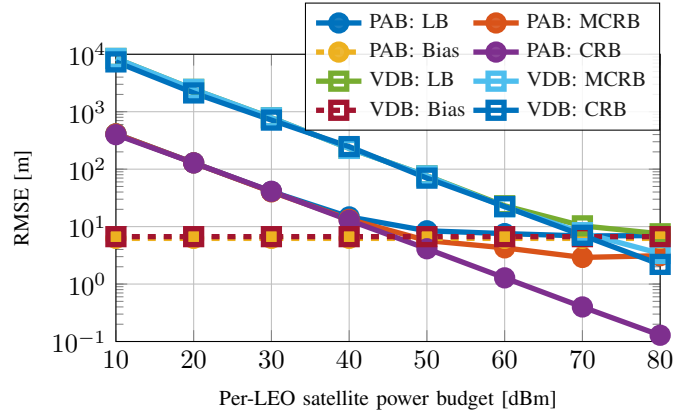


Fig. 5. Positioning RMSE LB versus per-LEO satellite power budget.

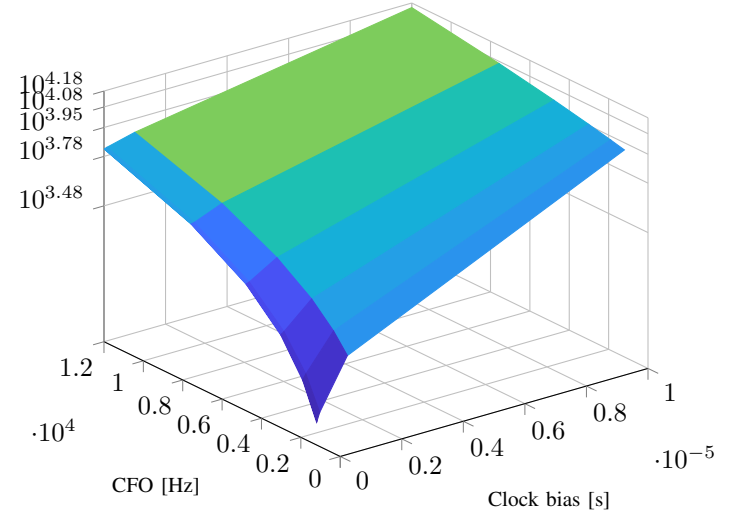


Fig. 6. Positioning RMSE LB versus maximum clock bias and CFO.

contrast, the LB with mismatch initially decreases but eventually saturates at a value determined by the bias, which remains independent of the transmit power. This emphasizes the detrimental impact of imperfect time- and frequency-synchronization among LEO satellites on positioning performance [24], [26], potentially leading to overly optimistic performance estimates. Moreover, compared to VDB, PAB achieves a lower LB, with the performance gain being more pronounced at lower (and more practical) transmit power levels. This advantage arises because PAB, by utilizing position information, can allocate more power to the UTs than VDB, underscoring the importance of integrating prior position knowledge into the positioning system.

As illustrated in Fig. 6, we further analyze the impact of varying time and frequency biases among satellite-UT pairs on positioning performance, resulting from imperfect time and frequency synchronization among LEO satellites. Specifically, we present the LB of positioning error (under PAB) as a function of the maximum clock bias and CFO values. The clock bias and CFO for each satellite-UT pair are uniformly distributed between 0 and their respective maximum values. The results reveal that positioning performance deteriorates

significantly as the maximum clock bias and CFO increase. A slight clock bias (on the order of milliseconds) or a minor CFO (on the order of $\Delta f/10$) can result in positioning errors of several kilometers, highlighting the critical importance of maintaining precise synchronization among LEO satellites in both time and frequency domains to achieve high-accuracy positioning.

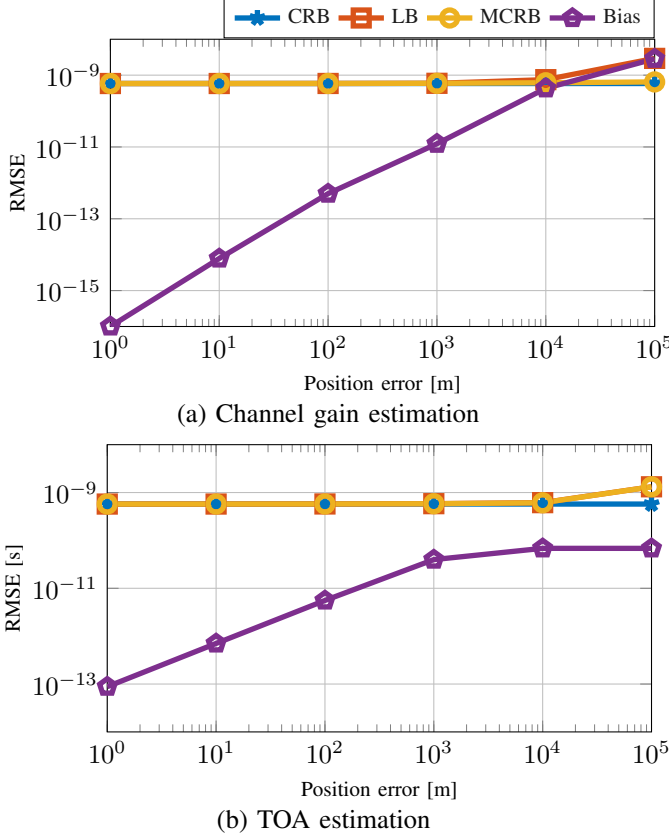


Fig. 7. Uplink channel estimation RMSE LB versus positioning error: (a) Channel vector estimation; (b) TOA estimation.

D. Uplink Channel Estimation

In Figs. 7(a) and (b), we evaluate the LB for both channel gain and TOA estimation RMSE using our proposed PACE across varying positioning errors, comparing it with Perfect-PACE (without positioning error-induced model mismatch). The results reveal that when positioning errors are small, PACE's LB closely matches that of Perfect-PACE for both parameters. However, as positioning errors increase, PACE's performance deteriorates due to growing model mismatch. For channel gain estimation, we observe that while the MCRB-induced error remains relatively insensitive to positioning errors, the bias component increases proportionally with positioning error, eventually becoming the primary contributor to overall channel gain error. The TOA estimation exhibits different behavior: its bias initially increases with positioning error before reaching a plateau, while the MCRB-induced error continues to grow, ultimately becoming the dominant factor in the total TOA estimation error. These findings underscore the importance of accurate downlink positioning

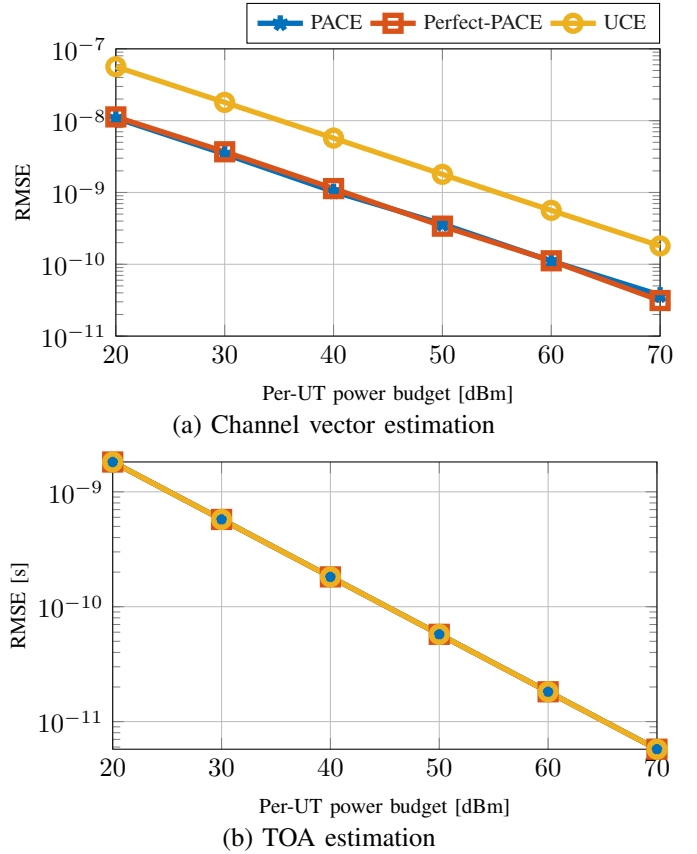


Fig. 8. Uplink channel estimation RMSE LB versus per-UT power budget: (a) Channel vector estimation; (b) TOA estimation.

in the first stage of PACE for achieving high-accuracy uplink channel estimation in the second stage.

In Figs. 8(a) and (b), we compare the LB for the RMSE of both channel vector and TOA estimation using the proposed PACE against those obtained under UCE, versus UT's power budget. Note that PACE estimates both the channel gain $\alpha_{s,u}$ and the TOA $\tau_{s,u}$, whereas UCE estimates the channel vector $\mathbf{h}_{s,u} = \alpha_{s,u}G(\theta_{s,u}^{\text{el}})\mathbf{a}(\theta_{s,u})$ (excluding the TOA-induced phase) in addition to $\tau_{s,u}$. To enable a unified comparison, we transform the LB for channel gain estimation RMSE in PACE into the corresponding LB for channel vector estimation RMSE (using the form $\hat{\mathbf{h}}_{s,u} = \hat{\alpha}_{s,u}G(\hat{\theta}_{s,u}^{\text{el}})\mathbf{a}(\hat{\theta}_{s,u})$) through algebraic manipulation. As shown, the TOA estimation performance of PACE closely aligns with that of UCE, exhibiting only negligible degradation due to positioning error. This alignment occurs because TOA estimation is independent of whether the other unknown parameter is the channel gain or the channel vector. This independence can be readily demonstrated by deriving the CRB for TOA estimation under Perfect-PACE and UCE, which we omit here due to space limitations. In contrast, PACE significantly outperforms UCE in channel vector estimation. This superiority is attributed to PACE's utilization of position information, which reduces the complexity of estimating a vector (as required by UCE) to that of estimating a scalar, albeit subject to positioning error. Consequently, PACE achieves higher channel estimation accuracy under the same pilot length and power budget.

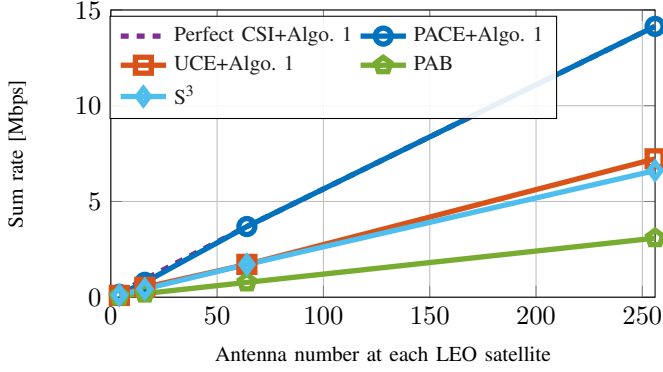


Fig. 9. Sum rate versus per-LEO satellite antenna number.

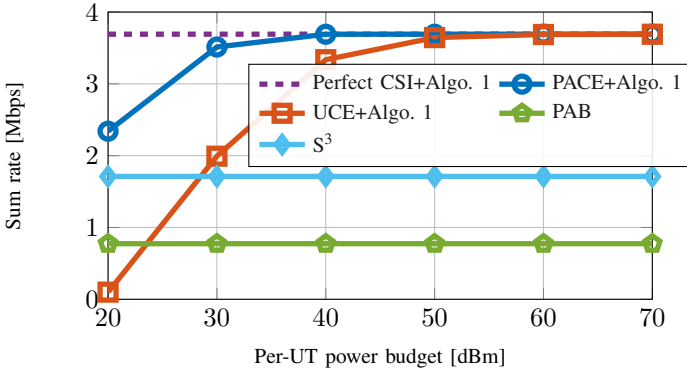


Fig. 10. Sum rate versus per-UT power budget.

E. Downlink Communication

In Fig. 9, we compare the downlink communication sum rates under various approaches versus the number of antennas equipped on each LEO satellite. As observed, the sum rate under the proposed PACE significantly outperforms those under UCE and other baselines, reaching a level very close to the sum rate with perfect CSI. This results from PACE's superior performance in reconstructing the channel accurately. Meanwhile, the sum rate under PAB is even lower than that under S^3 , underscoring the importance of accurate CSI in delivering the full capability of multi-LEO satellite downlink communication. Furthermore, with an increasing number of antennas on each LEO satellite, the performance gain of the proposed scheme becomes more evident, highlighting its potential in facilitating high-speed LEO satellite communication with massive antenna arrays.

As shown in Fig. 10, we compare the resultant sum rates under various schemes versus the per-UT power budget. It can be seen that the sum rates under PAB and S^3 are irrelevant to UTs' transmit power, while S^3 remains superior to PAB throughout the entire range. However, with increasing transmit power from the UT side, the sum rates under PACE and UCE increase and gradually approach those under perfect CSI. This is because the channel estimation accuracy under both schemes increases with higher transmit power, which translates into a sum rate gain. Nevertheless, the sum rate under PACE is significantly always higher than that under

UCE (especially notable when the transmit power at the UT is low). This highlights the importance of leveraging position information to obtain accurate CSI when the power budget at the UTs is limited, which is particularly relevant for equipments such as cell phones.

VI. CONCLUSION

This paper presents a novel framework for integrating positioning and communication in multi-LEO satellite systems, leveraging positioning capabilities to enhance channel estimation and thereby facilitate communication. By capitalizing on the distinct timescale variations of position-related parameters and channel gains, we propose a two-timescale frame structure that strategically schedules downlink positioning, uplink channel estimation, and downlink communication. A rigorous MCRB-based analysis characterizes the impact of practical imperfections, including inter-satellite clock bias and CFO, on positioning accuracy. Additionally, we theoretically demonstrate through MCRB analysis how position information improves uplink channel estimation even under inevitable positioning errors. To overcome the limited link budget offered by single-satellite-based downlink communication, we introduce a multi-satellite distributed beamforming strategy that relies on local CSI at each satellite, eliminating the need for centralized coordination. Numerical results validate our theoretical findings. As a direction for future work, developing practical algorithms and validating the framework through experimental testing would be valuable next steps.

APPENDIX A

DERIVATIVES OF $\tilde{\mathbf{f}}(\mathbf{r}_u)$ WITH RESPECT TO \mathbf{r}_u

1) Non-Zero First-Order Derivative:

$$\frac{\partial v_{s,u}}{\partial \mathbf{p}_u} = \frac{\mathbf{v}_s}{\lambda \|\mathbf{p}_u - \mathbf{p}_s\|} - \frac{(\mathbf{v}_s^\top (\mathbf{p}_u - \mathbf{p}_s)) (\mathbf{p}_u - \mathbf{p}_s)}{\lambda \|\mathbf{p}_u - \mathbf{p}_s\|^3},$$

$$\frac{\partial \tau_{s,u}}{\partial \mathbf{p}_u} = \frac{\mathbf{p}_u - \mathbf{p}_s}{c \|\mathbf{p}_u - \mathbf{p}_s\|}, \quad \frac{\partial v_{s,u}}{\partial \delta_u} = 1, \quad \frac{\partial \tau_{s,u}}{\partial b_u} = 1.$$

2) Non-Zero Second-Order Derivative:

$$\frac{\partial^2 v_{s,u}}{\partial \mathbf{p}_u^2} = -\frac{\mathbf{v}_s (\mathbf{p}_u - \mathbf{p}_s)^\top}{\lambda \|\mathbf{p}_u - \mathbf{p}_s\|^3} - \frac{\mathbf{v}_s (\mathbf{p}_u - \mathbf{p}_s)^\top + \mathbf{v}_s^\top (\mathbf{p}_u - \mathbf{p}_s) \mathbf{I}_3}{\lambda \|\mathbf{p}_u - \mathbf{p}_s\|^3},$$

$$+ \frac{3 (\mathbf{v}_s^\top (\mathbf{p}_u - \mathbf{p}_s)) (\mathbf{p}_u - \mathbf{p}_s) (\mathbf{p}_u - \mathbf{p}_s)^\top}{\lambda \|\mathbf{p}_u - \mathbf{p}_s\|^5},$$

$$\frac{\partial^2 \tau_{s,u}}{\partial \mathbf{p}_u^2} = \frac{\mathbf{I}_3}{c \|\mathbf{p}_u - \mathbf{p}_s\|} - \frac{(\mathbf{p}_u - \mathbf{p}_s) (\mathbf{p}_u - \mathbf{p}_s)^\top}{c \|\mathbf{p}_u - \mathbf{p}_s\|^3}.$$

APPENDIX B

DERIVATIVES OF $\tilde{\mathbf{g}}(\boldsymbol{\eta}_{s,u})$ WITH RESPECT TO $\boldsymbol{\eta}_{s,u}$

Note that the derivatives $\partial \tilde{\mathbf{g}}(\boldsymbol{\eta}_{s,u}) / \partial [\boldsymbol{\eta}_{s,u}]_i$ and $\partial^2 \tilde{\mathbf{g}}(\boldsymbol{\eta}_{s,u}) / (\partial [\boldsymbol{\eta}_{s,u}]_i \partial [\boldsymbol{\eta}_{s,u}]_j)$ can be constructed by concatenating $\partial \tilde{\mathbf{g}}_{s,u}[\ell, k] / \partial [\boldsymbol{\eta}_{s,u}]_i$ and $\partial^2 \tilde{\mathbf{g}}_{s,u}[\ell, k] / (\partial [\boldsymbol{\eta}_{s,u}]_i \partial [\boldsymbol{\eta}_{s,u}]_j)$, respectively, for $\ell = 1, \dots, L_c$ and $k = 1, \dots, K$. For simplicity, we provide the latter below.

1) *Non-Zero First-Order Derivative:*

$$\frac{\partial \tilde{\mathbf{g}}_{s,u}[\ell, k]}{\partial \Re\{\vartheta_{s,u}\}} = e^{-j2\pi k \Delta f \tau_{s,u}} \tilde{\mathbf{d}}_{s,u}[\ell, k],$$

$$\frac{\partial \tilde{\mathbf{g}}_{s,u}[\ell, k]}{\partial \Im\{\vartheta_{s,u}\}} = j e^{-j2\pi k \Delta f \tau_{s,u}} \tilde{\mathbf{d}}_{s,u}[\ell, k],$$

$$\frac{\partial \tilde{\mathbf{g}}_{s,u}[\ell, k]}{\partial \tau_{s,u}} = -\vartheta_{s,u} j 2\pi k \Delta f e^{-j2\pi k \Delta f \tau_{s,u}} \tilde{\mathbf{d}}_{s,u}[\ell, k].$$

2) *Non-Zero Second-Order Derivative:*

$$\frac{\partial^2 \tilde{\mathbf{g}}_{s,u}[\ell, k]}{\partial \Re\{\vartheta_{s,u}\} \partial \tau_{s,u}} = -j 2\pi k \Delta f e^{-j2\pi k \Delta f \tau_{s,u}} \tilde{\mathbf{d}}_{s,u}[\ell, k],$$

$$\frac{\partial^2 \tilde{\mathbf{g}}_{s,u}[\ell, k]}{\partial \Im\{\vartheta_{s,u}\} \partial \tau_{s,u}} = 2\pi k \Delta f e^{-j2\pi k \Delta f \tau_{s,u}} \tilde{\mathbf{d}}_{s,u}[\ell, k],$$

$$\frac{\partial^2 \tilde{\mathbf{g}}_{s,u}[\ell, k]}{\partial \tau_{s,u}^2} = -\vartheta_{s,u} (2\pi k \Delta f)^2 e^{-j2\pi k \Delta f \tau_{s,u}} \tilde{\mathbf{d}}_{s,u}[\ell, k].$$

REFERENCES

- [1] Y. Zhang *et al.*, “Challenges and opportunities of future rural wireless communications,” *IEEE Communications Magazine*, vol. 59, no. 12, pp. 16–22, 2021.
- [2] J. G. Andrews *et al.*, “6G takes shape,” *IEEE BITS the Information Theory Magazine*, pp. 1–38, 2024.
- [3] A. Papathanassiou *et al.*, “A comparison study of the uplink performance of W-CDMA and OFDM for mobile multimedia communications via LEO satellites,” *IEEE Personal Communications*, vol. 8, no. 3, pp. 35–43, 2001.
- [4] S. Liu *et al.*, “LEO satellite constellations for 5G and beyond: How will they reshape vertical domains?” *IEEE Communications Magazine*, vol. 59, no. 7, pp. 30–36, 2021.
- [5] J. Ma *et al.*, “Integrated positioning and communication via LEO satellites: Opportunities and challenges,” *arXiv preprint arXiv: 2411.14360*, 2024.
- [6] K.-X. Li *et al.*, “Channel estimation for LEO satellite massive MIMO OFDM communications,” *IEEE Transactions on Wireless Communications*, vol. 22, no. 11, pp. 7537–7550, 2023.
- [7] M. Khammassi *et al.*, “Precoding for high-throughput satellite communication systems: A survey,” *IEEE Communications Surveys & Tutorials*, vol. 26, no. 1, pp. 80–118, 2024.
- [8] A. M. Darya *et al.*, “Semi-blind channel estimation for massive mimo LEO satellite communications,” *IEEE Communications Letters*, vol. 29, no. 1, pp. 75–79, 2025.
- [9] P.-D. Arapoglou *et al.*, “MIMO over satellite: A review,” *IEEE Communications Surveys & Tutorials*, vol. 13, no. 1, pp. 27–51, 2011.
- [10] M. Y. Abdelsadek *et al.*, “Distributed massive MIMO for LEO satellite networks,” *IEEE Open Journal of the Communications Society*, vol. 3, pp. 2162–2177, 2022.
- [11] —, “Broadband connectivity for handheld devices via leo satellites: Is distributed massive MIMO the answer?” *IEEE Open Journal of the Communications Society*, vol. 4, pp. 713–726, 2023.
- [12] Z. Xiang *et al.*, “Massive MIMO downlink transmission for multiple LEO satellite communication,” *IEEE Transactions on Communications*, vol. 72, no. 6, pp. 3352–3364, 2024.
- [13] Y.-Y. He *et al.*, “Physical beam sharing for communications with multiple low earth orbit satellites,” *IEEE Transactions on Signal Processing*, vol. 72, pp. 2783–2798, 2024.
- [14] X. Zhang *et al.*, “Multi-satellite cooperative networks: Joint hybrid beamforming and user scheduling design,” *IEEE Transactions on Wireless Communications*, vol. 23, no. 7, pp. 7938–7952, 2024.
- [15] D. Kim *et al.*, “Coverage analysis of dynamic coordinated beamforming for LEO satellite downlink networks,” *IEEE Transactions on Wireless Communications*, vol. 23, no. 9, pp. 12239–12255, 2024.
- [16] R. Di Taranto *et al.*, “Location-aware communications for 5G networks: How location information can improve scalability, latency, and robustness of 5G,” *IEEE Signal Processing Magazine*, vol. 31, no. 6, pp. 102–112, 2014.
- [17] N. Gonzalez-Prelcic *et al.*, “Millimeter-wave communication with out-of-band information,” *IEEE Communications Magazine*, vol. 55, no. 12, pp. 140–146, 2017.
- [18] F. Jiang *et al.*, “Two-timescale transmission design and RIS optimization for integrated localization and communications,” *IEEE Transactions on Wireless Communications*, vol. 22, no. 12, pp. 8587–8602, 2023.
- [19] G. Kwon *et al.*, “Integrated localization and communication for efficient millimeter wave networks,” *IEEE Journal on Selected Areas in Communications*, vol. 41, no. 12, pp. 3925–3941, 2023.
- [20] G. Zhou *et al.*, “Individual channel estimation for RIS-aided communication systems—a general framework,” *IEEE Transactions on Wireless Communications*, vol. 23, no. 9, pp. 12038–12053, 2024.
- [21] S. Kim *et al.*, “Cell-free massive non-terrestrial networks,” *IEEE Journal on Selected Areas in Communications*, vol. 43, no. 1, pp. 201–217, 2025.
- [22] Z. M. Kassas *et al.*, “Ad astra: Simultaneous tracking and navigation with megaconstellation LEO satellites,” *IEEE Aerospace and Electronic Systems Magazine*, vol. 39, no. 9, pp. 46–71, 2024.
- [23] R. M. Ferre *et al.*, “Is LEO-based positioning with mega-constellations the answer for future equal access localization?” *IEEE Communications Magazine*, vol. 60, no. 6, pp. 40–46, 2022.
- [24] H. Xv *et al.*, “Joint beam scheduling and beamforming design for cooperative positioning in multi-beam LEO satellite networks,” *IEEE Transactions on Vehicular Technology*, vol. 73, no. 4, pp. 5276–5287, 2024.
- [25] P. Zheng *et al.*, “LEO- and RIS-empowered user tracking: A riemannian manifold approach,” *IEEE Journal on Selected Areas in Communications*, vol. 42, no. 12, pp. 3445–3461, 2024.
- [26] L. You *et al.*, “Integrated communications and localization for massive MIMO LEO satellite systems,” *IEEE Transactions on Wireless Communications*, vol. 23, no. 9, pp. 11061–11075, 2024.
- [27] S. Fortunati *et al.*, “Performance bounds for parameter estimation under misspecified models: Fundamental findings and applications,” *IEEE Signal Processing Magazine*, vol. 34, no. 6, pp. 142–157, Nov. 2017.
- [28] C. A. Balanis, *Antenna Theory: Analysis and Design*. Wiley-Interscience, 2005.
- [29] H. Wymeersch *et al.*, “Radio localization and sensing—part II: State-of-the-art and challenges,” *IEEE Communications Letters*, vol. 26, no. 12, pp. 2821–2825, 2022.
- [30] 3GPP, “Study on New Radio (NR) to support non-terrestrial networks,” 3rd Generation Partnership Project, Technical Report TR 38.811, 2020, release 15.
- [31] W. Liu *et al.*, “Effect of turbulence layer height and satellite altitude on tropospheric scintillation on Ka-band Earth-LEO satellite links,” *IEEE Transactions on Vehicular Technology*, vol. 59, no. 7, pp. 3181–3192, 2010.
- [32] R. M. Zaeem *et al.*, “Synchronization errors and SINR performance: How critical are they in cell-free massive MIMO with ultra-dense LEO satellite connectivity?” in *IEEE 99th Vehicular Technology Conference (VTC2024-Spring)*, 2024, pp. 1–5.
- [33] F. Kunzi *et al.*, “Precise onboard time synchronization for LEO satellites,” *NAVIGATION: Journal of the Institute of Navigation*, vol. 69, no. 3, 2022.
- [34] F. S. Prol *et al.*, “Position, navigation, and timing (PNT) through low earth orbit (LEO) satellites: A survey on current status, challenges, and opportunities,” *IEEE Access*, vol. 10, pp. 83971–84002, 2022.
- [35] C. Ozturk *et al.*, “RIS-aided localization under pixel failures,” *IEEE Transactions on Wireless Communications*, vol. 23, no. 8, pp. 8314–8329, 2024.
- [36] Q. Shi *et al.*, “An iteratively weighted MMSE approach to distributed sum-utility maximization for a MIMO interfering broadcast channel,” *IEEE Transactions on Signal Processing*, vol. 59, no. 9, pp. 4331–4340, 2011.
- [37] International Telecommunication Union, “Attenuation by atmospheric gases and related effects,” International Telecommunication Union, Geneva, Recommendation P.676-12, 2019.
- [38] A. Hourani. (2024) Atmospheric absorption loss for satellite communications. [Online]. Available: <https://www.mathworks.com/matlabcentral/fileexchange/78865atmospheric-absorption-loss-for-satellite-communications>
- [39] A. Al-Hourani *et al.*, “On modeling satellite-to-ground path-loss in urban environments,” *IEEE Communications Letters*, vol. 25, no. 3, pp. 696–700, 2021.
- [40] S. Gezici *et al.*, “Ranging in a single-input multiple-output (SIMO) system,” *IEEE Communications Letters*, vol. 12, no. 3, pp. 197–199, 2008.